

Molecule lifetimes vs. molecular cloud lifetimes: accretion dominates

Sarah M. R. Jeffreson¹, Vadim Semenov¹ and Mark R. Krumholz^{2,3}

¹ Center for Astrophysics, Harvard & Smithsonian, 60 Garden St, Cambridge, MA 02138, USA

² Research School of Astronomy and Astrophysics, Australian National University, Canberra, ACT 2611 Australia

³ Australian Research Council Centre of Excellence for All Sky Astrophysics in 3 Dimensions (ASTRO 3D), Australia

Accepted XXX. Received XXX; in original form XXX

ABSTRACT

Abstract.

Key words: ISM:clouds – ISM:evolution – ISM: structure – ISM: Galaxies – Galaxies: star formation

1 INTRODUCTION

In recent years a dynamical picture of star formation has emerged, whereby gas undergoes ‘rapid cycles’ of star formation into the star-forming state and is then ejected by feedback.

If star formation cycles are so short, then how can simulated GMCs be so long-lived? How do massive GMCs form at all, when parcels of size XXX are destroyed on time-scales 5–15 Myr and constantly cycling? Some authors have proposed that very large molecular regions are destroyed as fast as the parcels that make them up.

In both Galactic and extragalactic sources, molecular gas is observed to be organised into discrete giant molecular clouds (GMCs). The masses, densities and velocity dispersions of these GMCs vary across several orders of magnitude. In the Milky Way, the range is XXX, and the properties of these clouds depend on the large-scale galactic environment (PHANGS). The range of typical observed GMC lifetimes is XXX—several times the observed time-scale of gas expulsion from around young massive stars (Krujssen+ 19, Chevance+ 20, Kim+ 20)—and . The most massive GMCs host a significant fraction of galactic star formation (Murray).

In order to model the rate and distribution of star formation and stellar feedback in the context of the wider galactic environment, it is necessary to understand the relationship between short, stellar feedback-driven cycles of star formation ($\sim 3\text{--}15$ Myr) and the evolution of the host GMCs ($\sim 3\text{--}100$ Myr). In this paper, we will use a numerical simulation of an isolated galaxy in the moving-mesh code AREPO to directly compare the chemical survival time of molecular hydrogen (t_{H_2}) to the lifetime of its host GMC (t_{GMC}). In particular, we will examine (1) how t_{GMC} and t_{H_2} are related, and (2) whether the local depletion time of molecular gas depend on the observable mass and lifetime of its host GMC. Addressing these questions will lead us to examine the GMC lifecycle as a function of the rate of accretion of gas into an H₂ molecule-dominated phase, versus the rate of ejection of gas from this state by stellar feedback.

To examine the detailed evolution of gas on sub-cloud scales, we require a high-resolution simulation with H₂ chemistry, stellar feedback and tracer particles. We describe the implementation of these physics in Section 2. In Section 3 we examine the explicit rela-

tionship between the GMC lifetime and the chemical survival time of molecular gas. We also address the depletion time. In Section 4 we look at the impact of the GMC distribution on the clustering of supernova feedback, observed to drive outflows. In Section 5 we use this information to propose a simple parametrisation of GMC evolution in terms of accretion (driven by the large-scale galactic environment) and ejection (driven by stellar feedback inside the GMCs). Such a model will be useful as a sub-grid model for star formation with a realistic distribution and environmental dependence.

2 ISOLATED DWARF SPIRAL GALAXY SIMULATION

We simulate a dwarf flocculent spiral galaxy that is analogous in its gas and stellar mass distribution to the bulgeless nearby galaxy NGC300. Figure 1 shows the spatial distribution of the total (left), atomic (centre-left), total molecular (centre-right) and CO-luminous molecular (right) gas reservoirs at face-on and edge-on viewing angles, at a simulation time of 800 Myr. The initial condition includes a dark matter halo at a mass resolution of $1.254 \times 10^7 \text{ M}_\odot$, a stellar disc at a mass resolution of $3.437 \times 10^3 \text{ M}_\odot$, and a gas disc at a mass resolution of 859 M_\odot . The dark matter halo follows the profile of Navarro et al. (1997), with a concentration parameter of $c = 15.4$, a spin parameter of $\lambda = 0.04$, a mass of $8.3 \times 10^{10} \text{ M}_\odot$ and a circular velocity of $V_{200} = 76 \text{ km s}^{-1}$ at the virial radius. The stellar disc is of exponential form, with a mass of $1 \times 10^9 \text{ M}_\odot$, a scale-length of 1.39 kpc, and a scale-height of 0.28 kpc. The corresponding exponential gas disc extends beyond the stellar disc, with a mass of $2.2 \times 10^9 \text{ M}_\odot$ (giving a gas fraction of 68 per cent) and a scale-length of 3.44 kpc.

The initial condition is evolved using the moving-mesh hydrodynamics code AREPO (Springel 2010). Within AREPO, the hydrodynamical (gaseous) component is modelled by the unstructured moving mesh defined by the Voronoi tessellation about a discrete set of points, which move according to the local gas velocity. The gravitational acceleration vectors of the Voronoi gas cells, stellar particles and dark matter particles are computed using a hybrid TreePM gravity solver.

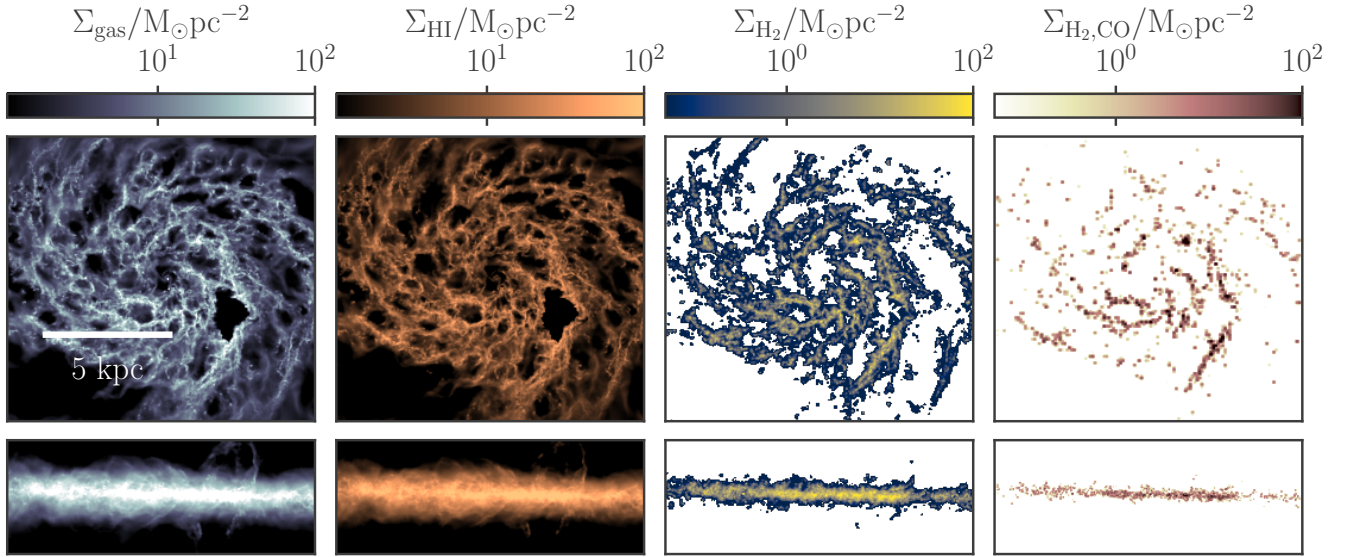


Figure 1. Column density maps of the total (Σ_{gas} , left), atomic (Σ_{HI} , centre-left), total molecular (Σ_{H_2} , centre-right), and CO-luminous molecular ($\Sigma_{\text{H}_2,\text{CO}}$) gas distribution for the simulated galaxy, viewed perpendicular to (top panels) and across (lower panels) the galactic mid-plane, at a simulation time of 800 Myr.

The temperature and chemical composition of the gas in our simulation is modelled using the simplified network of hydrogen, carbon and oxygen chemistry described in Nelson & Langer (1997) and in Glover & Mac Low (2007a,b). The fractional abundances of the chemical species H, H_2 , H^+ , He, C^+ , CO, O and e^- are computed and tracked for each gas cell, and self-consistently coupled to the heating and cooling of the interstellar medium via the atomic and molecular cooling function of Glover et al. (2010). The gas equilibrates to a state of thermal balance between line-emission cooling and heating due to the photo-electric emission from polycyclic aromatic hydrocarbons and dust grains, as they interact with the interstellar radiation field (ISRF) and with cosmic rays. We assign a value of 1.7 Habing fields to the UV component of the ISRF (Mathis et al. 1983), a value of $3 \times 10^{-17} \text{ s}^{-1}$ to the cosmic ray ionisation rate (van der Tak & van Dishoeck 2000), and we assume the solar value for the dust-to-gas ratio. We note that this results in a higher metallicity than the sub-solar value that is observed for NGC300 (Bresolin et al. 2009).

We use the TREECOL algorithm introduced by Clark et al. (2012) to model the dust- and self-shielding of molecular hydrogen from dissociation by the ISRF. This allows us to accurately model the non-equilibrium abundance of molecular hydrogen during the run-time of the simulation, and so to compute its value for each gas cell as a function of time.

We introduce passive tracer particles to the simulation following the Monte Carlo prescription of Genel et al. (2013), which allows us to track the Lagrangian mass flow and molecular fraction of gas as it moves through simulated GMCs, despite the fact that AREPO is not a Lagrangian code. Via this prescription, tracer particles are moved along with the gas cells in the simulation, and are exchanged between gas cells according to a probability set by the mass flux between them. When a gas cell is converted to a star particle, the tracer particles associated with that gas cell are moved to the star particle with a probability set by the ratio of the stellar mass to the original gas cell mass. Similarly, tracer particles attached to star particles are transferred back to the gas reservoir according to

the masses ejected in stellar winds and supernovae. As such, the mass of tracers in the gas and stellar reservoirs remains equal to the masses of these reservoirs throughout the simulation. In this work, we assign one tracer particle to each gas cell in the initial condition, which sets an initial mass distribution for the tracer particles, equal to the initial mass distribution of gas cells. We compute the error associated with this initial mass distribution in Appendix 7, and show that when averaged over hundreds of tracer particles (as in this work), the traced mass fluxes converge to those expected for a uniform initial distribution of tracer masses.

The star formation efficiency ϵ_{ff} per free-fall time of the gas in our simulations follows the parametrisation of Padoan et al. (2017). These authors conduct high-resolution simulations of turbulent fragmentation and find that ϵ_{ff} depends on the local virial parameter α_{vir} of the gas, according to

$$\epsilon_{\text{ff}} = 0.4 \exp(-1.6\alpha_{\text{vir}}^{0.5}). \quad (1)$$

Our simulations do not include a sub-grid model for turbulence, and so we follow the prescription of Gensior et al. (2020) to determine the length-scale L of the local over-density, across which α_{vir} is calculated. In brief, L is set to $|\langle \rho_g \rangle / \langle \nabla \rho_g \rangle|$, where $\langle \nabla \rho_g \rangle$ is the cubic spline kernel-weighted average of the gas volume density gradient, with respect to the radial distance from the central gas cell. The smoothing length of the cubic spline kernel is chosen to enclose the 32 nearest-neighbour cells. We refer the reader to Gensior et al. (2020) for a more detailed explanation. The star formation rate volume density of each gas cell in the simulation is therefore given by

$$\frac{d\rho_{*,i}}{dt} = \begin{cases} \frac{\epsilon_{\text{ff}}\rho_i}{t_{\text{ff},i}}, & \rho_i \geq \rho_{\text{thresh}}, T_i \leq T_{\text{thresh}} \\ 0, & \rho_i < \rho_{\text{thresh}}, T_i > T_{\text{thresh}} \end{cases}, \quad (2)$$

where $t_{\text{ff},i} = \sqrt{3\pi/(32G\rho_i)}$ is the local free-fall time-scale for the gas cell i with a mass volume density of ρ_i , and ϵ_{ff} is given by Equation (1).

We set a lower limit of $\rho_{\text{thresh}}/m_{\text{H}}\mu = 100 \text{ cm}^{-3}$ on the volume

density of hydrogen atoms above which star formation is allowed to occur, as well as an upper limit of $T_{\text{thresh}} = 100 \text{ K}$ on the temperature. The value of ρ_{thresh} is the density of Jeans-unstable (collapsing) gas at our mass resolution of 859 M_\odot and at the temperature of $\sim 30 \text{ K}$ reached by the molecular gas in our simulation. For a spherical gas cell, the radius associated with this density threshold is 3 pc, and so we employ the adaptive gravitational softening scheme in AREPO with a minimum softening length of 6 pc and a gradation of 1.5 times the Voronoi gas cell diameter. We set the softening length of the stellar particles to the same value, and choose a softening length of 280 pc for the dark matter particles, according to the convergence tests presented in Power et al. (2003). Because our simulations resolve the gas disc scale-height and the Toomre mass at all scales, the adaptive gravitational softening avoids the majority of artificial fragmentation at scales larger than the Jeans length (Nelson 2006).

To each star particle formed during the simulation, we assign a stellar population drawn stochastically from a Chabrier (2003) initial stellar mass function (IMF), using the Stochastically Lighting Up Galaxies (SLUG) stellar population synthesis model (da Silva et al. 2012, 2014; Krumholz et al. 2015). Within SLUG, the resulting stellar populations are evolved along Padova solar metallicity tracks (Fagotto et al. 1994a,b; Vázquez & Leitherer 2005) during run-time, using STARBURST99-like spectral synthesis (Leitherer et al. 1999). This modelling provides the number of supernovae $N_{*,\text{SN}}$ generated by each star particle during each simulation time-step, as well as the ionising luminosity of the cluster and the mass Δm_* it has ejected.

We use the values of $N_{*,\text{SN}}$ and Δm_* for each star particle to compute the momentum and thermal energy injected by supernova explosions at each time-step. In the case of $N_{*,\text{SN}} = 0$, we assume that all mass loss results from stellar winds. In the case of $N_{*,\text{SN}} > 0$, we assume that all mass loss results from supernova explosions, and we model the corresponding kinetic and thermal energy injection due to the expanding blast-wave. At our mass resolution of 500 M_\odot per gas cell, the energy-conserving/momentum-generating phase of supernova blast-wave expansion is unresolved, and so we follow the prescription introduced by Kimm & Cen (2014): we explicitly inject the terminal momentum of the blast-wave into the set of gas cells k that share faces with the nearest-neighbour cell to the star particle. We use the unclustered parametrisation of the terminal momentum derived from the high-resolution simulations of Gentry et al. (2017), which is given by

$$\frac{p_{t,k}}{\text{M}_\odot \text{ km s}^{-1}} = 4.249 \times 10^5 N_{*,\text{SN}} \left(\frac{n_k}{\text{cm}^{-3}} \right)^{-0.06}, \quad (3)$$

with an upper limit imposed by the condition of kinetic energy conservation, as the shell sweeps through the gas cells k . The momentum is distributed among the facing cells as described in Jeffreson et al. (2021b).

The pre-supernova feedback from HII regions is implemented according to the model of Jeffreson et al. (2021b). This model accounts both for the momentum injected by radiation pressure, and for the momentum injected by the thermal pressure from the heated gas inside the ionised bubble, following the analytic work of Matzner (2002); Krumholz & Matzner (2009). Momentum is injected for groups of star particles with overlapping ionisation-front radii, which are identified using a Friends-of-Friends grouping prescription. The momentum is received by the gas cell closest to the luminosity-weighted centre of the Friends-of-Friends group, and is distributed to the set of adjoining neighbour cells. The gas cells inside the Strömgren radii of each Friends-of-Friends group are heated to a temperature of 7000 K, and are held above this

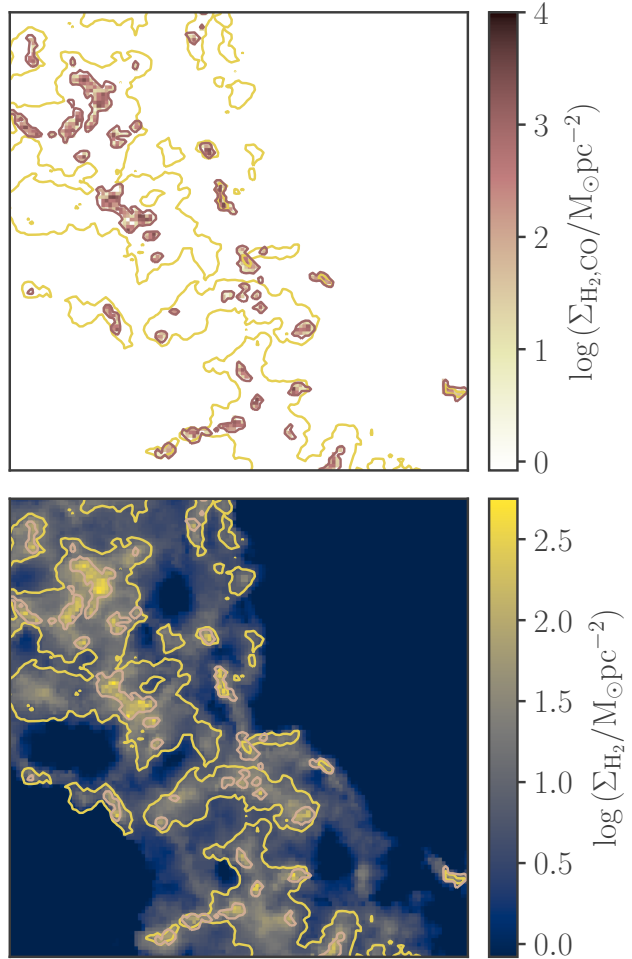


Figure 2. Our thresholds for the identification of star-forming regions, using the projected H_2 fraction $\Sigma_{\text{H}_2}/\Sigma_{\text{gas}}$ (yellow contours) and the CO-luminous molecular gas surface density $\Sigma_{\text{H}_2,\text{CO}}$ (pink contours). Our threshold of $\Sigma_{\text{H}_2}/\Sigma_{\text{gas}} = 0.3$ is chosen to enclose the same total mass M_{H_2} of the total galactic molecular hydrogen as would be enclosed by the commonly-used threshold $\Sigma_{\text{H}_2} = 10 \text{ M}_\odot \text{ pc}^{-2}$ on the molecular gas surface density. Our threshold of $\log(\Sigma_{\text{H}_2,\text{LCO}}/\text{M}_\odot \text{ pc}^{-2}) = -1.5$ on the CO-luminous H_2 surface density is chosen according to our chemical post-processing, as described in Section 3.1.

temperature floor for as long as they receive ionising photons from the group. In contrast to Jeffreson et al. (2021b), we also explicitly and fully ionise the gas inside these Strömgren radii, rather than relying on the chemical network to do so.

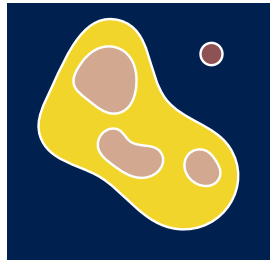
3 STAR-FORMING REGIONS IN $^{12}\text{CO } J = 1 \rightarrow 0$ AND IN TOTAL H_2 ABUNDANCE

In this section, we describe our procedure for identifying star-forming regions at each instant in our simulation, and tracking these regions as they evolve over time. We use the passive tracer particles in the simulation to partition the gas into its CO-luminous and CO-dark components, and to study their evolution and star formation separately.

Table 1. The instantaneous gas mass (upper table) and stellar mass formed (lower table) in four different gas reservoirs, which partition the total gas reservoir of the simulated galaxy. The reservoirs are illustrated in the lower schematic image. Pink corresponds to CO-luminous gas that also has a projected molecular gas fraction above 0.3. Yellow corresponds to the CO-dark envelope, with a projected molecular gas fraction above 0.3. Dark pink corresponds to CO-luminous gas with a low projected molecular gas fraction < 0.3. Dark blue corresponds to gas that is neither CO-luminous nor molecular gas-rich.

Gas reservoir	Av. instantaneous gas mass	% of galactic gas mass	% of molecular gas mass
CO-luminous, $\Sigma_{\text{H}_2}/\Sigma_{\text{gas}} > 0.3$	$4.4 \times 10^7 M_{\odot}$	2.3	26.0
CO-dark, $\Sigma_{\text{H}_2}/\Sigma_{\text{gas}} > 0.3$	$6.3 \times 10^7 M_{\odot}$	3.3	30.1
CO-luminous, $\Sigma_{\text{H}_2}/\Sigma_{\text{gas}} < 0.3$	$1.9 \times 10^6 M_{\odot}$	0.1	0.5
CO-dark, $\Sigma_{\text{H}_2}/\Sigma_{\text{gas}} < 0.3$	$1.8 \times 10^9 M_{\odot}$	94.3	43.4

Gas reservoir	Stellar mass formed/Myr	% of galactic stellar mass formed	Integrated SFE over 300 Myr
CO-luminous, $\Sigma_{\text{H}_2}/\Sigma_{\text{gas}} > 0.3$	$5.3 \times 10^5 M_{\odot}$	77.5	0.012
CO-dark, $\Sigma_{\text{H}_2}/\Sigma_{\text{gas}} > 0.3$	$1.2 \times 10^5 M_{\odot}$	16.6	0.0021
CO-luminous, $\Sigma_{\text{H}_2}/\Sigma_{\text{gas}} < 0.3$	$3.0 \times 10^2 M_{\odot}$	0.04	1.2×10^{-4}
CO-dark, $\Sigma_{\text{H}_2}/\Sigma_{\text{gas}} < 0.3$	$4.0 \times 10^4 M_{\odot}$	5.7	2.2×10^{-5}



3.1 Identification of star-forming regions at each instant in time

Observationally, star-forming regions are most-commonly identified as ‘giant molecular clouds’ traced by the $J = 1 \rightarrow 0$ rotational emission line from ^{12}CO molecules that are mixed with the cold molecular hydrogen gas. However, ^{12}CO molecules are dissociated by lower-energy radiation (~ 8 eV) than are H_2 molecules ($\gtrsim 11.2$ eV Draine 1978), such that there also exists a reservoir of ‘CO-dark’ H_2 . Observations in the solar neighbourhood (e.g. Grenier et al. 2005; Paradis et al. 2012) and dedicated numerical simulations of Milky Way-like galaxies estimate that CO-dark H_2 may account for half the mass of the molecular hydrogen reservoir (?).

In this work, we identify both CO-bright, observable star-forming regions, as well as star-forming regions delineated by their total H_2 abundance, which contain a CO-dark component. The former are identified using isocontours of value $\log(\Sigma_{\text{H}_2,\text{CO}}/\text{M}_{\odot}\text{pc}^{-2}) = -1.5$, where $\Sigma_{\text{H}_2,\text{CO}}$ is the surface density of CO-bright molecular hydrogen perpendicular to the galactic mid-plane. This threshold corresponds to the natural break in the distribution of $\Sigma_{\text{H}_2,\text{CO}}$ produced by our chemical post-processing, which is described in detail in Appendix 7. On one side of the threshold are gas cells that contain at least some shielded, CO-dominated gas. On the other side, CO exists only as a uniformly-mixed, unshielded, low-abundance component. Our second population of star-forming regions are enclosed within isocontours of value $\log(\Sigma_{\text{H}_2}/\Sigma_{\text{gas}}) = 0.3$, where Σ_{H_2} is the molecular hydrogen surface density and Σ_{gas} is the total gas surface density. These contours enclose the same total mass of galactic H_2 ($7 \times 10^7 M_{\odot}$) as would be enclosed by the commonly-used threshold of $\Sigma_{\text{H}_2} = 10 \text{ M}_{\odot}\text{pc}^{-2}$ on the total molecular hydrogen surface density.

In Figure 2 we show examples of both isocontours ($\Sigma_{\text{H}_2,\text{CO}}$ in pink, Σ_{H_2} in yellow) for a $(3 \text{ kpc})^2$ section of the simulated

interstellar medium. These are overlaid onto maps of $\Sigma_{\text{H}_2,\text{CO}}$ (top panel) and Σ_{H_2} (bottom panel). We see that the CO-bright molecular hydrogen exists as regions of higher-density H_2 within envelopes of more-diffuse, CO-dark H_2 .

3.2 Star formation CO-bright regions and CO-dark envelopes using tracer particles

Using the tracer particles in our simulation, we may track the evolution of Lagrangian gas parcels over time, through both CO-luminous and CO-dark molecular gas. We assign a tracer to a star-forming region at time t if it falls within the bounding isocontour of $\Sigma_{\text{H}_2,\text{CO}}$ or $\Sigma_{\text{H}_2}/\Sigma_{\text{gas}}$ for the region, as specified in Section 3.1. We also require a molecular hydrogen abundance of $x_{\text{H}_2} > 10^{-5}$, to remove tracers far from the galactic mid-plane.

In Table 1, we show the partitioning of the simulated gas reservoir into four: gas that is H_2 -rich and CO-luminous (pink, 2.3 per cent by mass), gas that is H_2 -rich but CO-dark (yellow, 3.3 per cent by mass), gas that is CO-luminous but H_2 -poor (dark red, 0.1 per cent by mass) and gas that is neither CO-luminous nor H_2 -rich (dark blue, 94.3 per cent by mass). The schematic below illustrates the typical distribution of gas in each reservoir in the galactic mid-plane, which can also be seen in Figure 2. The CO-dark molecular hydrogen is typically distributed in an envelope around embedded regions of CO-bright molecular hydrogen.

Using the gas tracer particles, we can also determine the percentage of star formation that occurs in each of the four gas reservoirs, given in the lower section of Table 1. To compute the first three rows of this table, we flag tracer particles that are associated with CO-luminous and H_2 -rich star-forming regions at time t , and take the intersection and differences between these sets. We compute the fraction of tracers in each set that are passed from gas cells to star particles during the following time-step. We take the average

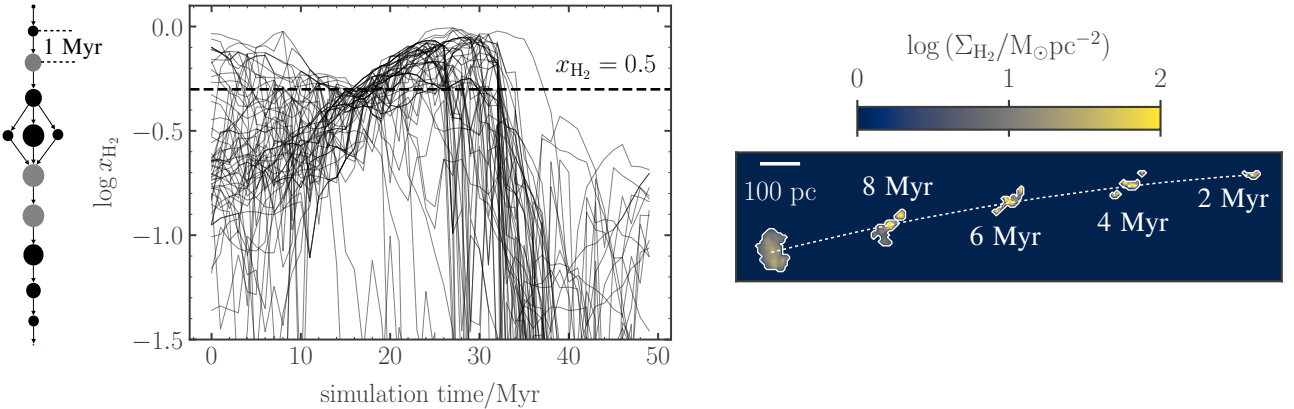


Figure 3. The lifecycle of a single simulated star-forming region, including both CO-bright gas and a CO-dark H₂ envelope. This region survives for 11 Myr, and undergoes a split and re-merger 4 Myr after its birth, with its evolution described by the network component on the left-hand side. The diameters of the nodes in the network are scaled according to the logarithm of the total H₂ mass, and time runs from the top to the bottom of the page in steps of 1 Myr. The corresponding evolution of the H₂ abundance for the tracer particles that transit through the star-forming region is shown in the central panel. The shape and H₂ surface density of the region are shown at five times in the right-hand panel, at five different times during its evolution.

of this fraction over all simulation times $t = 500\text{--}800$ Myr. The final row of the table is computed by taking the union of tracer particles in the CO-luminous and H₂-rich star-forming regions, subtracting these from the total set of tracer particles for the whole simulation, and computing the conversion fraction from gas to stars of what remains.

Table 1 demonstrates that both the CO-luminous and CO-dark H₂-rich gas reservoirs are interesting with respect to star formation. The CO-luminous molecular hydrogen accounts for 78 per cent of all star formation in the simulation. The CO-dark envelope accounts for just 17 per cent of star formation, but over 60 per cent of the total galactic molecular gas mass.

The CO-dark fraction is higher and the overall molecular gas fraction is lower than in the Milky Way, which is expected for a dwarf spiral galaxy that is analogous to NGC300. XXX add phase diagram, highlighting these four gas reservoirs. Add citations for the CO-dark fraction and molecular gas fraction of the Milky Way XXX.

In what follows, we will examine these two gas reservoirs in greater detail, separating the gas parcels that transit through CO-luminous star-forming regions from those that reach only the CO-dark envelope, and are expelled before reaching the CO-luminous phase.

3.3 Tracking the evolution and lifetimes of star-forming regions

We use a novel technique for measuring the end-to-end evolution of star-forming regions, while accounting for the intervening mergers and splits of their interacting parts, described in detail in [Jefferson et al. \(2021a\)](#).

In brief, the positions of the two-dimensional isocontour enclosing a star-forming region at simulation time t is projected forward by the time-step $\Delta t = 1$ Myr of our simulation output, using the velocities of the gas cells in the region. A pair of star-forming regions is temporally linked as parent and child if there exists any

overlap between the projected contour of the parent at time t and the contour outlining the child at time $t + \Delta t$.

The resulting *cloud evolution network* contains many mergers and splits of molecular regions, due to the turbulent, fractal nature of the molecular interstellar medium. However, we find that the network for CO-luminous regions is made up of ~ 8000 distinct, complete, non-interacting segments between simulation times of $t = 500$ and 800 Myr, and between galactocentric radii of $R = 2$ and 6 kpc. These segments correspond to independent star-forming regions. Segments are only considered complete if they do not touch the specified limits in t and R , and are temporally-resolved with a length of at least 1 Myr. This representative sub-sample of star-forming regions with complete, temporally-resolved evolution corresponds to 15 per cent of the molecular mass of the entire population identified in Section 3.1. It has a total mass of $\sim 10^7 M_\odot$.

An example of one such independent star-forming region, with a peak mass of $5 \times 10^4 M_\odot$, is shown in Figure 3. On the left-hand side of the figure we show the corresponding segment of the cloud evolution network, where time runs from top to bottom in steps of 1 Myr. The region splits into three and re-merges between ages 4 and 6 Myr. The diameter of each node node is scaled as the logarithm of the total H₂ mass at each time, and grey-coloured nodes indicate time-steps at which stars are formed inside the cloud. The central panel shows the evolution of the molecular hydrogen abundance x_{H_2} for each tracer particle that enters the star-forming region during its evolution. The right-hand panel shows the molecular hydrogen surface density within the isocontour defining the cloud at five different times during its evolution.

Figure 3 illustrates that at any one time, an independent star-forming region may be made up of several neighbouring but spatially-separated parts that were split apart by stellar feedback at an earlier time, and may re-merge again at a later time. Regions of lower mass (a few $10^4 M_\odot$) may be made up of just one molecular region at all times, but the temporal evolution is always more complex for higher-mass regions, often containing many mergers and splits.

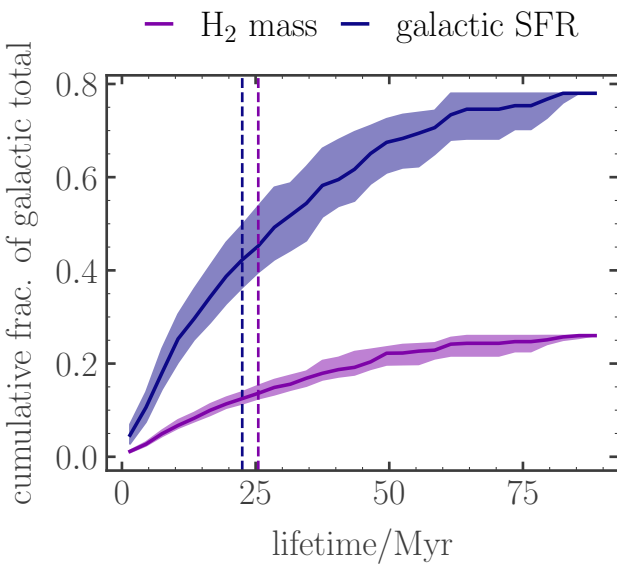


Figure 4. Time-averaged cumulative fraction of the total galactic molecular mass and star formation rate (SFR) accounted for by GMCs of different lifetimes. The solid lines denote the time-averaged median values over the 300-Myr interval in simulation time analysed, while the shaded regions denote the corresponding interquartile ranges. Both cumulative fractions are normalised to the total molecular mass of the GMC sub-sample for which the GMC lifetime is temporally-resolved and complete.

3.4 The galactic distribution of GMC masses and lifetimes

Note that the sub-sample of GMCs with complete time evolution within the simulation time interval we examine is only 11 per cent. However, we expect this to be a representative sub-sample, because the simulation interval examined is long (300 Myr) and the GMC population is steady/in equilibrium after 500 Myr of disc warm-up.

4 THE CYCLING OF GAS THROUGH H₂-RICH STAR-FORMING REGIONS

In this section, we take the population of gas tracer particles that transit through each CO-luminous star-forming region in our simulation and examine the evolution of these gas parcels as a function of the lifetimes of their host regions. In Section 3 we have shown that CO-luminous star-forming regions account for 78 per cent of star formation in the simulated galaxy.

4.1 The survival time of H₂ vs. the survival time of its host star-forming region

We find that gas tracer particles cycle constantly in and out of a H₂-rich state, in qualitative agreement with the results presented by Semenov et al. (2017). We use a threshold on the molecular hydrogen abundance of $x_{\text{H}_2} = 0.5$ to measure the length of these cycles. In the upper left panel of Figure 5, we show the duration and median H₂ abundance for tracer particles in the H₂-rich state, with $x_{\text{H}_2} \geq 0.5$, coloured according to the mean lifetime of their host star-forming regions. The percentage of tracers that pass through multiple star-forming regions decreases from 23 per cent for the

shortest-lived regions down to 9 per cent for the longest-lived regions. We consider all complete cycles of gas parcels that transit through star-forming regions over all simulation times between 500 and 800 Myr.

In Figure 5 we see that the time spent by gas parcels in the H₂-rich phase is short, ranging from 1 to 20 Myr with a median value of 3 Myr. This short time-scale is consistent with the disruption of molecular gas by pre-supernova stellar feedback, which we will discuss in the next section. The median abundance of molecular hydrogen over the duration of each cycle is 0.63. Crucially, the cycles are identical in duration and form for gas tracers in star-forming regions of any lifetime. That is, across all star-forming regions, gas is consistently pushed out of the H₂-rich state on a time-scale of ~ 3 Myr.

By contrast, in the upper right panel of Figure 5, we see that the behaviour of gas parcels in the CO-poor state is (weakly) dependent on the lifetime of the host star-forming region. The time-scales shown here are all lower limits, as we consider all periods of $x_{\text{H}_2} < 0.5$, including those that abut the time limits of the simulation at $t = 500$ and $t = 800$ Myr. Gas parcels that are associated with shorter-lived star-forming regions are ejected for longer periods of time into the H₂-poor phase, and reach lower median H₂ abundances. Because the median time spent with $x_{\text{H}_2} < 0.5$ for these gas parcels is substantially longer than the lifetimes of their host regions, we can deduce that the ejection of the gas parcels from the H₂-rich state is associated with the complete destruction of the region, and so the total removal of self-shielding for any remaining H₂. By contrast, the time spent with $x_{\text{H}_2} < 0.5$ for gas parcels in long-lived (high-mass) star-forming regions is shorter than the region lifetime: a degree of self-shielding remains from the remaining molecular gas in the extended structure, and so the return to the H₂-rich phase is faster.

The lower panel of Figure 5 shows the total time spent by gas parcels in the H₂-rich state, over the 300 Myr interval of simulation time considered. We see that gas parcels transiting through long-lived star-forming regions spend approximately double the time with $x_{\text{H}_2} \geq 0.5$ than do gas parcels travelling through the shortest-lived regions. The tracer particles spend cumulative total of 26 Myr in the H₂-rich state for a mean region lifetime equal to 90 Myr, corresponding to ~ 8 individual cycles of median length 3 Myr. In star-forming regions of mean lifetime < 10 Myr, they spend a cumulative total of only 13 Myr with $x_{\text{H}_2} \geq 0.5$.

We therefore find that the local environment provided by a star-forming region has a weak impact on the survival time of H₂ molecules in that region. A factor 20 difference in the lifetime of a CO-luminous star-forming region corresponds to just a factor 6 increase in the median time spent by gas in an H₂-rich state. In Figure 6 we demonstrate that this increase in the survival time of cold, shielded molecular hydrogen corresponds to a factor 3 increase in the integrated star formation efficiency between the shortest-lived clouds (10 Myr, 0.006) and the longest-lived clouds (58 Myr, 0.035). We have shown in Figure 4 that

4.2 The efficiency of destruction of H₂ by stellar feedback

In Section 4.1 we showed that molecular gas is less-efficiently disrupted in longer-lived star-forming regions, leading to a greater amount of time spent in the H₂-rich state. In Figure XXX we demonstrate that this is due primarily to the greater degree of H₂ self-shielding provided by larger, more-massive star-forming regions. The correspondence between the mass of star-forming regions and their lifetimes was demonstrated in Figure 4.

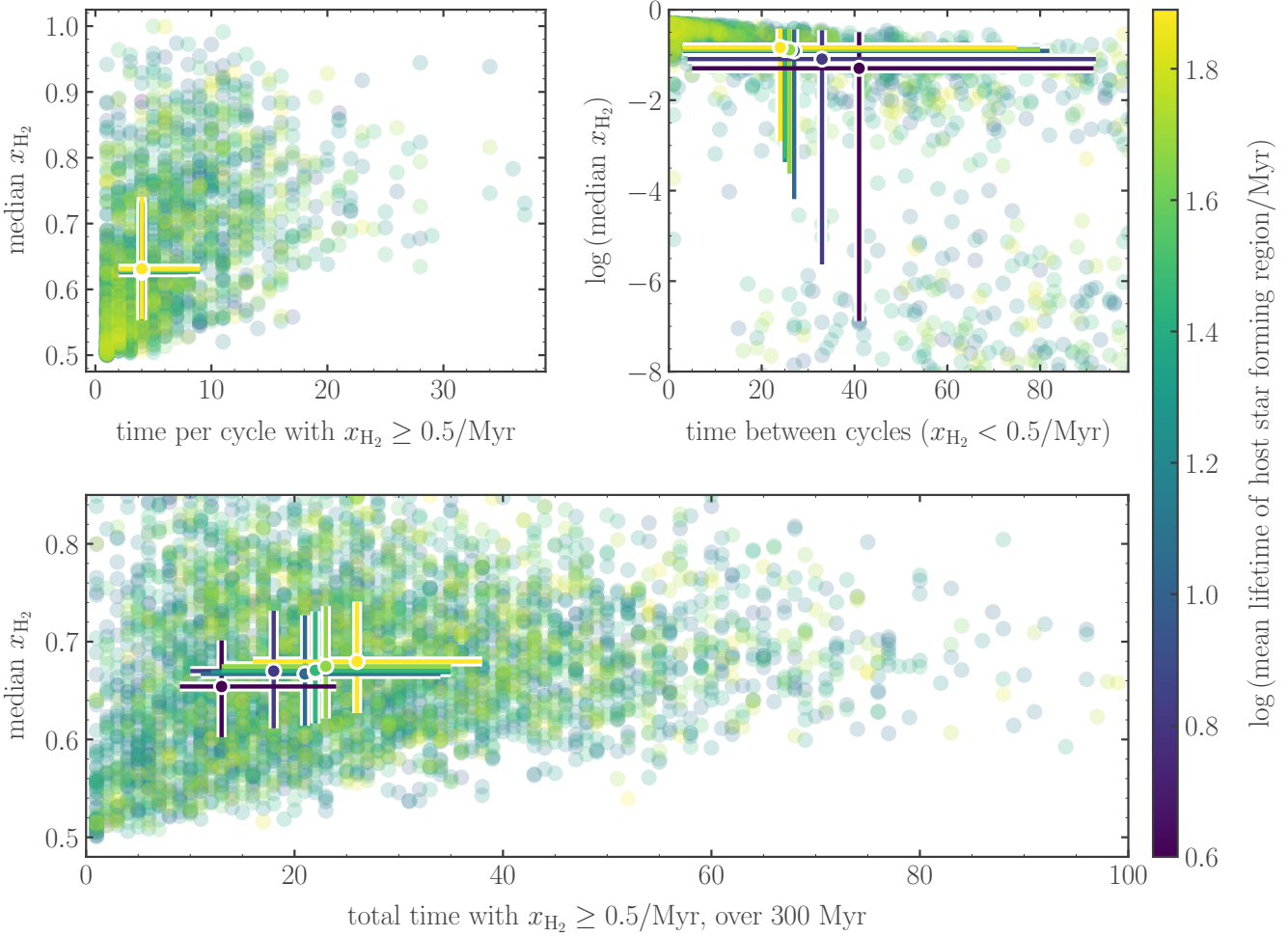


Figure 5. The time spent by gas tracer particles in the H_2 -rich ($x_{\text{H}_2} \geq 0.5$) and H_2 -poor ($x_{\text{H}_2} < 0.5$) phases, for tracer particles that transit through CO-luminous star-forming regions. The transparent data points give the values for 1/5000th of the tracer particles, while the solid data points and lines give the median values and interquartile ranges along each axis. All points are coloured according to the lifetime of the star-forming region through which they transit. The upper two panels give the durations of individual cycles, while the lower panel gives the total time spent in the H_2 -rich phase, for each tracer particle.

5 CLOUD EVOLUTION IS DRIVEN BY ACCRETION VS. EJECTION

In the previous section we have also seen that tracer cycles are much shorter than cloud lifetimes, and even the tracer particles that remain molecular the longest still contribute their weight for less than a quarter of the lifetime of the host region.

The above results present a chicken-and-egg situation. Do some clouds reach longer lifetimes and higher masses because they are more difficult to destroy? Or do clouds become more difficult to destroy once they have reached a higher mass? What actually determines whether or not a cloud is able to reach a high mass?

Here, the answer comes from considering the conditions at formation of the star-forming region. The peak cloud mass (and therefore lifetime) is determined by the time at which the rate of final ejection of gas from the molecular-dominated state (after it has completed its final cycle) becomes equal to the rate of accretion of new gas. This depends on the mass the cloud has obtained before stars are formed and stellar feedback sets in. We have seen that molecular gas is 2–3 times more difficult to destroy in clouds that obtain higher masses, due to the higher density and abundance of

molecular gas around the star-forming regions, and so the higher the degree of self-shielding. So if a cloud obtains a higher mass before feedback sets in,

In this section, we investigate whether the relative rates of mass accretion and feedback-driven ejection can provide a simple formula for the GMC mass as a function of time (and consequently the GMC lifetime). Such a prescription may ultimately be used to provide a semi-analytic sub-resolution model of GMC evolution and star formation in simulations that do not resolve individual GMCs.

5.1 The mass evolution of GMCs

In the upper panel of Figure 9 we show the medians (solid lines) and interquartile ranges (shaded regions) of the masses of all GMCs in our sample as a function of time. These GMCs have been identified via a threshold on the molecular gas surface density, as described in Section 2. They are divided into five bins according to their maximum masses, as indicated by colour. The minimum mass at which GMCs appear is limited by the mass resolution of our simulation, which is $900 M_\odot$. The pattern of mass increase to its maximum, followed by a decrease until the end of the cloud lifetime, is univer-

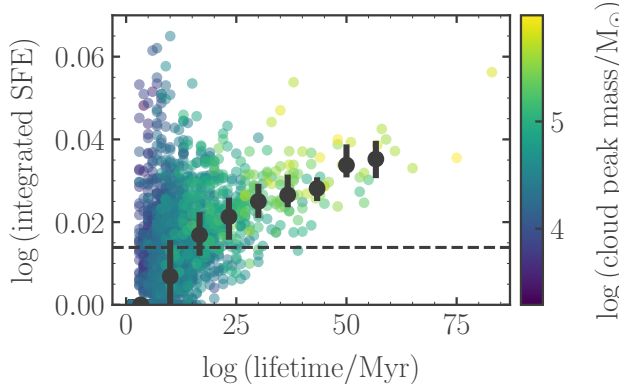


Figure 6. Integrated star formation efficiency over the lifetime of a CO-luminous star-forming region, as a function of the lifetime of the star-forming region. The black data points and error bars correspond to the median values and interquartile ranges in each lifetime interval. The horizontal dashed line gives the total stellar mass produced in all regions divided by the total mass of all regions, which is equal to the total SFE within the simulation (see Table 1), as expected. The transparent data points correspond to the values for individual star-forming regions, coloured by the peak mass they attain during their lifetimes.

sal, gradual, and roughly-symmetrical across the simulated GMC population.

In the lower panel of Figure 9, we show the rates of accretion and ejection of molecular mass to (solid lines) and from (dashed lines) the GMC population in the same mass bins, as a function of time. At each time, the accreted mass is calculated as the using the masses of the gas tracers associated with the GMC footprint (see Section 2) that have entered a state of high molecular gas fraction $x_{\text{H}_2} \geq 0.5$ during the previous time-step, multiplied by their current molecular fractions. These masses are summed for each GMC. The ejected mass is calculated similarly using the masses of the gas tracers that dropped below $x_{\text{H}_2} = 0.5$ during the previous time-step, multiplied by their current molecular fractions.

Comparison of the upper and lower panels of Figure 9 demonstrates that the peak GMC mass corresponds approximately to the time at which the rates of molecular mass accretion and ejection are equal. Similarly, the end of the GMC lifetime corresponds approximately to the time after which the total ejected molecular mass equals the total accreted molecular mass (given by the areas under the curves in the lower panel).

In Figure ??, we demonstrate that the median GMC lifetime is directly predicted by the time after cloud formation at which the total molecular mass ejected from the cloud is equal to the total mass accreted ($t(M_{\text{accretion}} = M_{\text{ej}})$, lower panel). The black solid line gives the gradient of direct proportionality. In the upper panel, we demonstrate that the pattern of GMC accretion and dispersal is roughly-symmetrical: the time $t(\dot{M}_{\text{accr}} = \dot{M}_{\text{ej}})$ at which the rate of molecular mass accretion and ejection are equal occurs at approximately half the GMC lifetime, at all GMC masses. Finally, the central panel of Figure ?? demonstrates that the instantaneous GMC mass is a simple linear function of the total molecular masses accreted and ejected.

We can therefore write the following simple formulae describ-

ing the evolution of GMCs in our simulation:

$$\begin{aligned} M(t) &= M_{\text{accr}}(t) - M_{\text{ej}}(t) \\ M(t_{\text{life}}) &= t(M_{\text{accr}} = M_{\text{ej}}) \\ M_{\text{peak}} &= t(\dot{M}_{\text{accr}} = \dot{M}_{\text{ej}}) \end{aligned} \quad (4)$$

5.2 What drives the ejection of molecular mass?

Here we will examine how the ejection rate correlates with the energy from HII regions and (separately) with SNe as a function of GMC mass. That is, show that the smaller GMCs are destroyed by HII regions, while the larger GMCs are destroyed by SNe.

6 DISCUSSION

Need to say that if we had properly-adjusting metallicity, the results might be different due to the effects of dust shielding.

7 CONCLUSIONS

ACKNOWLEDGEMENTS

We thank Volker Springel for providing us access to Arepo. SMRJ is supported by Harvard University through the ITC. The work was undertaken with the assistance of resources and services from the National Computational Infrastructure (NCI; award jh2), which is supported by the Australian Government. We are very grateful to Shy Genel, Greg Bryan, Blakesley Burkhardt and Enrique Vázquez-Semadeni for helpful discussions.

DATA AVAILABILITY STATEMENT

The data underlying this article are available in the article and in its online supplementary material.

REFERENCES

- Bresolin F., Gieren W., Kudritzki R.-P., Pietrzyński G., Urbaneja M. A., Carraro G., 2009, *ApJ*, **700**, 309
- Chabrier G., 2003, *PASP*, **115**, 763
- Clark P. C., Glover S. C. O., Klessen R. S., 2012, *MNRAS*, **420**, 745
- Draine B. T., 1978, *ApJS*, **36**, 595
- Fagotto F., Bressan A., Bertelli G., Chiosi C., 1994a, *A&AS*, **104**, 365
- Fagotto F., Bressan A., Bertelli G., Chiosi C., 1994b, *A&AS*, **105**, 29
- Genel S., Vogelsberger M., Nelson D., Sijacki D., Springel V., Hernquist L., 2013, *MNRAS*, **435**, 1426
- Gensior J., Kruijssen J. M. D., Keller B. W., 2020, arXiv e-prints, [p. arXiv:2002.01484](https://arxiv.org/abs/2002.01484)
- Gentry E. S., Krumholz M. R., Dekel A., Madau P., 2017, *MNRAS*, **465**, 2471
- Glover S. C. O., Mac Low M.-M., 2007a, *ApJS*, **169**, 239
- Glover S. C. O., Mac Low M.-M., 2007b, *ApJ*, **659**, 1317
- Glover S. C. O., Federrath C., Mac Low M. M., Klessen R. S., 2010, *MNRAS*, **404**, 2
- Grenier I. A., Casandjian J.-M., Terrier R., 2005, *Science*, **307**, 1292
- Jeffreson S. M. R., Keller B. W., Winter A. J., Chevance M., Kruijssen J. M. D., Krumholz M. R., Fujimoto Y., 2021a, *MNRAS*, **505**, 1678
- Jeffreson S. M. R., Krumholz M. R., Fujimoto Y., Armillotta L., Keller B. W., Chevance M., Kruijssen J. M. D., 2021b, *MNRAS*, **505**, 3470
- Kimm T., Cen R., 2014, *ApJ*, **788**, 121
- Krumholz M. R., Matzner C. D., 2009, *ApJ*, **703**, 1352

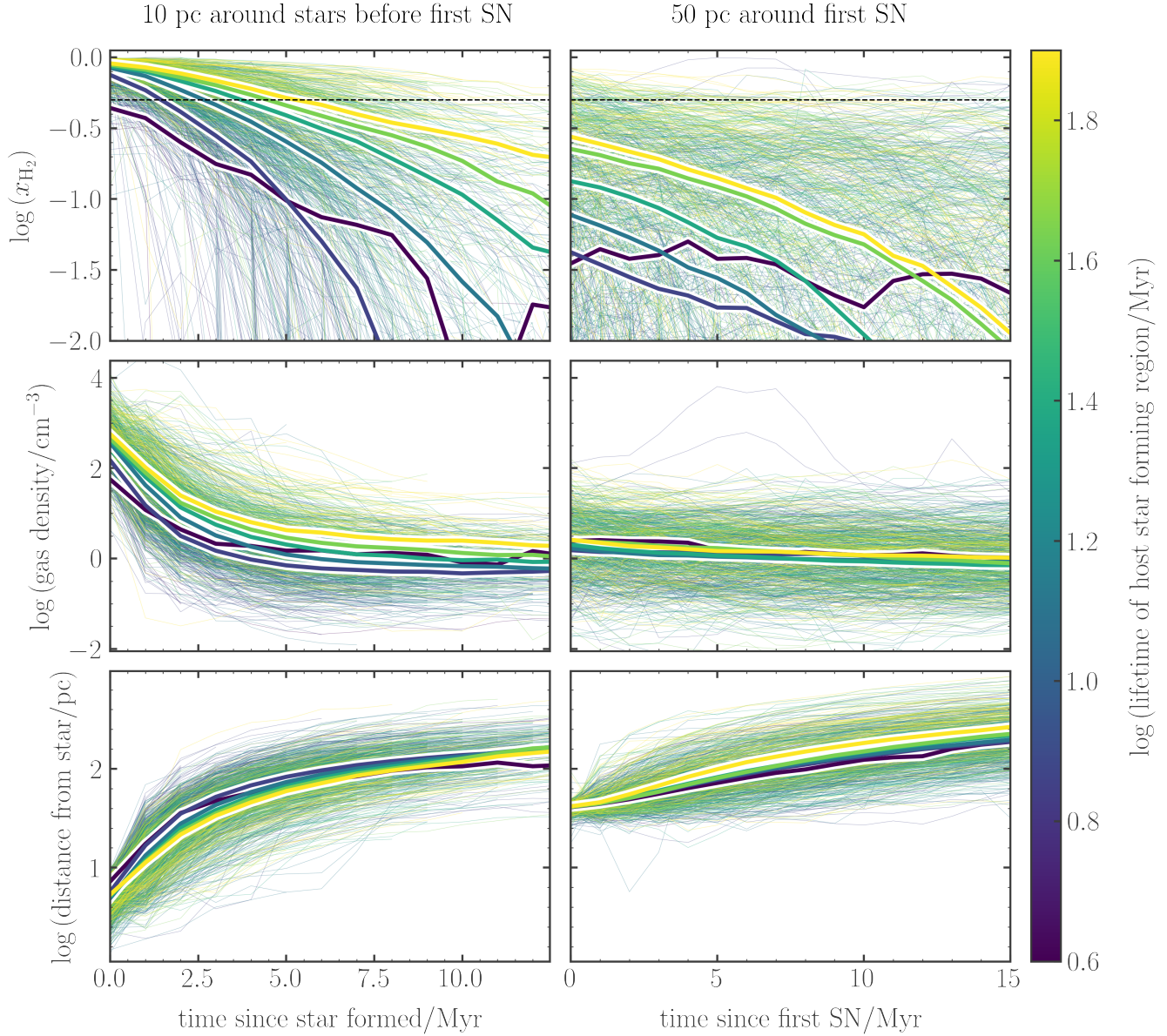


Figure 7.

- Krumholz M. R., Fumagalli M., da Silva R. L., Rendahl T., Parra J., 2015, *MNRAS*, **452**, 1447
 Leitherer C., et al., 1999, *ApJS*, **123**, 3
 Mathis J. S., Mezger P. G., Panagia N., 1983, *A&A*, **500**, 259
 Matzner C. D., 2002, *ApJ*, **566**, 302
 Navarro J. F., Frenk C. S., White S. D. M., 1997, *ApJ*, **490**, 493
 Nelson A. F., 2006, *MNRAS*, **373**, 1039
 Nelson R. P., Langer W. D., 1997, *ApJ*, **482**, 796
 Padoa P., Haugbølle T., Nordlund Å., Frimann S., 2017, *ApJ*, **840**, 48
 Paradis D., Dobashi K., Shimoikura T., Kawamura A., Onishi T., Fukui Y., Bernard J. P., 2012, *A&A*, **543**, A103
 Power C., Navarro J. F., Jenkins A., Frenk C. S., White S. D. M., Springel V., Stadel J., Quinn T., 2003, *MNRAS*, **338**, 14
 Semenov V. A., Kravtsov A. V., Gnedin N. Y., 2017, *ApJ*, **845**, 133
 Springel V., 2010, *MNRAS*, **401**, 791
 Vázquez G. A., Leitherer C., 2005, *ApJ*, **621**, 695
 da Silva R. L., Fumagalli M., Krumholz M., 2012, *ApJ*, **745**, 145

da Silva R. L., Fumagalli M., Krumholz M. R., 2014, *MNRAS*, **444**, 3275
 van der Tak F. F. S., van Dishoeck E. F., 2000, *A&A*, **358**, L79

Error associated with the initial mass distribution of tracers
 Chemical post-processing

This paper has been typeset from a $\text{\TeX}/\text{\LaTeX}$ file prepared by the author.

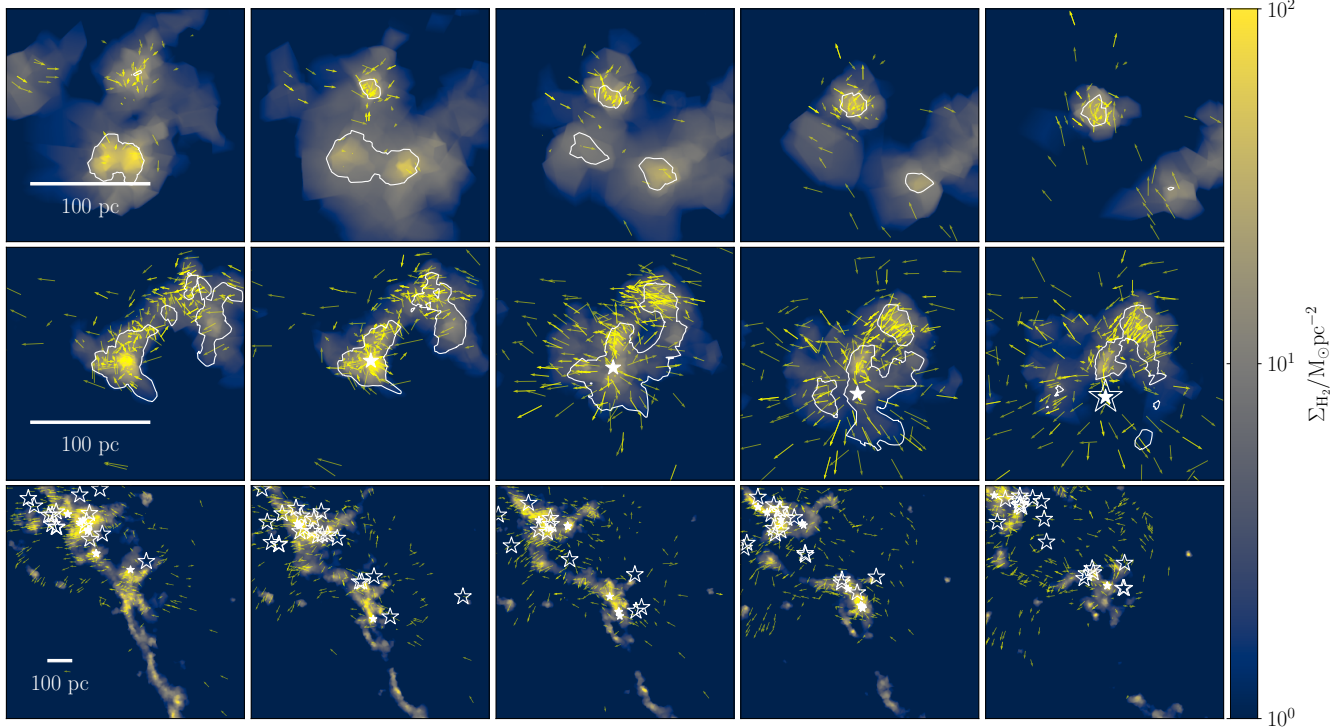
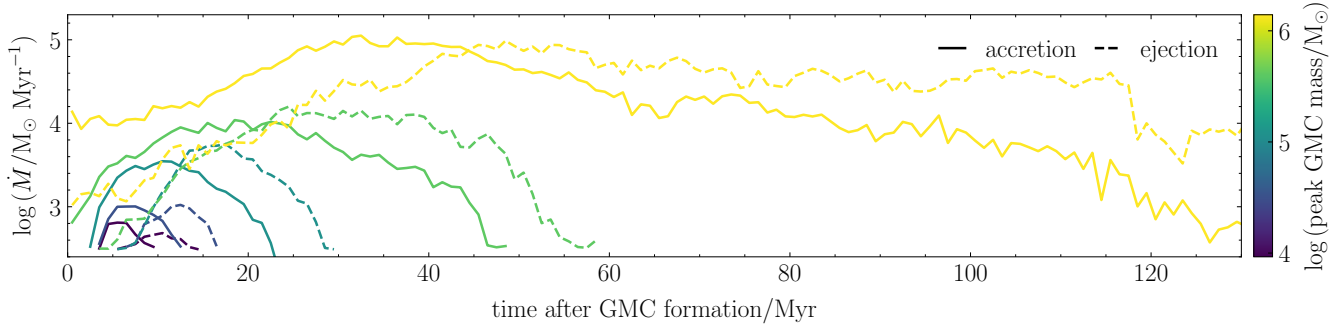
**Figure 8.**

Figure 9. The simulated GMCs follow a symmetrical pattern of mass evolution from formation to destruction, driven by the competition between accretion and ejection of molecular mass. Here we show the median molecular mass of gas parcels accreted into (solid lines) and ejected from (dashed lines) a state of molecular fraction $x_{\text{H}_2} > 0.5$ for the entire GMC population of the simulated galaxy, divided into five mass bins with centres indicated by colour. These GMC populations are identical to those presented in Figure ??.

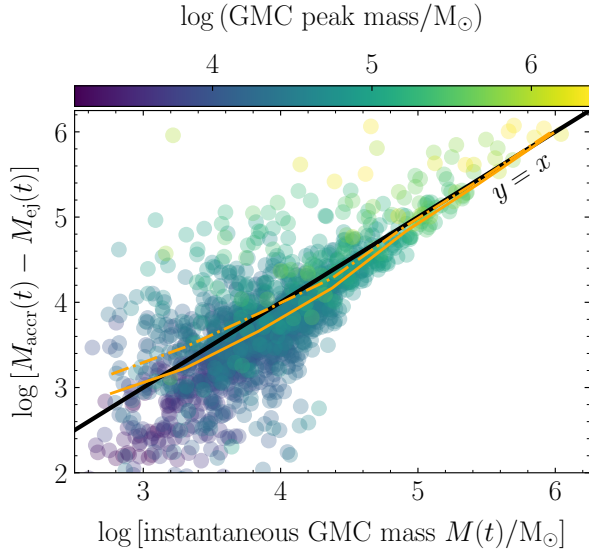


Figure 10. The instantaneous GMC mass $M(t)$ can be predicted as a simple function of the cumulative mass $M_{\text{accr}}(t)$ accreted to the molecular-dominated state $x_{\text{H}_2} \geq 0.5$, relative to the cumulative mass M_{ej} ejected. Here we show the net molecular mass accumulated into the molecular-dominated state, as a function of the instantaneous (observable) GMC mass. Transparent points show 1/50th of the values for all GMCs in the simulated population, while the solid orange line represents the median of all values in bins of the instantaneous GMC mass. As for Figure ??, the dot-dashed orange line represents the median value when we additionally include the evolution of gas parcels within ± 25 Myr of the GMC lifetime. By comparing the solid and dot-dashed lines, we see that our selection of gas parcels does not significantly bias the trend.